RSC Advances

PAPER

View Article Online
View Journal | View Issue

Cite this: *RSC Adv.*, 2014, **4**, 63408

Simultaneous doping and growth of Sn-doped hematite nanocrystalline films with improved photoelectrochemical performance†

Guosheng Ruan,[a] Shouliang Wu,[a] Panpan Wang,[a] Jun Liu,[a] Yunyu Cai,[a] Zhenfei Tian,[a] Yixing Ye,[a] Changhao Liang*[a] and Guosheng Shao[b]

Hematite is an important material used in water splitting and lithium-ion battery electrodes. Electronic conductivity and the visible light-absorption ability of hematite are enhanced by doping impurity ions into the hematite lattice and achieving an appropriate hematite nanostructure. This paper reports the simultaneous doping and growth of tin (Sn)-doped hematite crystalline films on a conducting substrate. The crystalline films were prepared by a hydrothermal process. Laser ablation in liquid induced SnO_x colloidal nanoparticles, which were used as the doping source. The obtained compacted films were characterized by scanning electron microscopy, transmission electron microscopy, X-ray diffraction (XRD), X-ray photoelectron spectroscopy, and UV-vis spectrophotometry analyses. XRD results showed the Sn-doped α-Fe_2O_3 crystalline nanoparticles had dominant active (110) planes. Annealing affected the photoelectrochemical (PEC) performance of the Sn-doped hematite photoanode, and the photocurrent density of the photoanode annealed at 750 °C for 2 h reached the highest value at 0.48 mA cm^{-2} (at 1.23 V *vs.* reversible hydrogen electrode). Electrochemical impedance spectroscopy measurements revealed that the charge-transfer resistance of Sn-doped hematite films decreased after the annealing treatment. The improved crystallinity and the preferred (110) plane in the doped crystalline film are favor of the migration of electrons and holes to electrode surfaces, the removal of deleterious surface states and increase of the free electron density, which should contribute to the enhanced PEC performance.

Received 25th October 2014
Accepted 14th November 2014

DOI: 10.1039/c4ra13124j

www.rsc.org/advances

Introduction

Solar energy utilization and conversion into storable energy has been proposed to address the increasing global energy demand. Photoelectrochemical (PEC) cells based on photoactive semiconductors may be used to realize this process.[1–5] Hematite has received considerable attention in photochemical H_2O oxidation because of its outstanding chemical stability in an aqueous environment, wide availability, and appropriate band gap for visible light. Theoretical prediction states that solar-to-hydrogen conversion efficiency of hematite may reach 16.8% and the attainable water-splitting photocurrent may be up to 12.6 mA cm^{-2}; these values are sufficient for practical applications.[6–9] However, hematite exhibits disadvantages that include poor conductivity,[10] short carrier-diffusion length,[11] and improper band position for water splitting.[12] These properties would cause an undesirable PEC performance of hematite during practical applications.

To overcome such disadvantages, several efforts have been made to improve the PEC performance of hematite. These efforts include changing the synthesis method, controlling product morphology, and introducing impurities to increase conductivity among others.[13–16] To date, various routes to prepare hematite photoanodes, such as magnetron sputtering,[17] sol–gel,[18] hydrothermal[19] and atmosphere pressure-chemical vapor deposition have been reported.[13,20] For significant enhancement in PEC performance, by changing the synthesis method and combined with doping of hetero-atoms is used to adopt.[3,8] Hematite is an n-type semiconductor because of the presence of naturally occurring O_2 vacancies in its bulk. Tetravalent foreign ions are introduced to substitute trivalent iron ions, forming an n-type doping of hematite. This form is easier to ionize completely, or it forms a covalent bond with O_2. Formation of covalent bonds with O_2 increases the number of charge carriers and improves electron conductivity. Numerous tetravalent dopants, such as Si,[3,21] Ti,[20,22,23] Ge,[24,25] and Sn[26–28] have been introduced in a hematite lattice. Except for key roles of appropriate dopants and structure of hematite, post-thermal treatment of a product is necessary to remove additional organics, decrease interfacial resistance, and increase crystallinity and uniformity of a hematite structure. For

[a]*Key Laboratory of Materials Physics, Institute of Solid State Physics, Hefei Institutes of Physical Science, Chinese Academy of Sciences, Hefei 230031, China. E-mail: chliang@issp.ac.cn; Fax: +86 551 65591434; Tel: +86 551 65591129*

[b]*Institute for Renewable Energy and Environmental Technologies, University of Bolton, Bolton BL3 5AB, UK*

† Electronic supplementary information (ESI) available. See DOI: 10.1039/c4ra13124j

instance, Sivula *et al.*[29] reported that thermal treatment of iron oxide (Fe_2O_3) films at a high temperature (800 °C) induced diffusion of Sn atoms from a transparent fluorine-doped SnO_2 (FTO) substrate. This occurrence resulted in increased PEC performance from *ca.* 10 μA cm^{-2} to 0.56 mA cm^{-2} at 1.23 V [*vs.* reversible hydrogen electrode (RHE)]. Ling *et al.*[13] found that photocurrent densities of Sn-doped hematite nanocorals improved at high annealing temperatures, and highest photocurrent density of 1.86 mA cm^{-2} at 1.23 V (*vs.* RHE) was achieved by annealing films at 800 °C for 20 min. Xi *et al.*[30] showed that a specific thermal treatment of iron oxyhydroxides (β-FeOOH) nanorods at 750 °C produced a $Fe_xSn_{1-x}O_4$ layer at the surface, which reduced electron–hole recombination at the hematite–electrolyte interface. Such high annealing temperatures have resulted in damage of the surface layer of a conducting substrate and possible inter-diffusion and reaction between hematite and substrate materials. Thus, the underlying reason for the improvement of PEC performance is still unclear. In this study, a well-grown Sn-doped hematite nanocrystalline film was used to investigate the effects of annealment on the interfacial modification of electrode materials and substrate, migration, possible reaction of dopants and bulk hematite, and the PEC performance of a Sn-doped hematite film. All these parameters were investigated to provide valuable evidence for the practical application of hematite materials in water splitting and lithium-ion electrode.

Experimental

Preparation of growth seed layer

Exactly 30 mL of an aqueous solution containing 0.405 g of $FeCl_3 \cdot 6H_2O$ and 0.650 g of $NaNO_3$ was placed in a 50 mL Teflon-lined stainless-steel autoclave. A piece of pre-cleaned glass with a transparent conducting oxide (FTO) layer was used as substrate and sealed into the autoclave. A uniform yellow layer of iron oxyhydroxides (β-FeOOH) formed on the FTO substrate surface after heating the autoclave at 120 °C for 5 h. The β-FeOOH films were then washed with deionized H_2O several times to remove residual ions.

Sn-doped hematite films

Sn-doped hematite photoelectrodes were synthesized through a designed fabrication strategy, as shown in Scheme 1. The Sn doping source, which was different from a common doping source, was generated by laser ablation in liquid (LAL) technique. A Sn target (>99.99%) was immersed in 15 mL of deionized H_2O in a cell. This target was ablated at designated durations by a 1064 nm Nd:YAG pulse laser (with pulse duration of 10 ns and pulse energy of 120 mJ). A gray SnO_x colloidal solution was obtained after 20 min. This solution was used as the Sn doping source. The prepared SnO_x colloidal solution was then homogeneously mixed with 5 mL of $FeCl_3$ (10 mM) solution. Around 10 mL of deionized H_2O was added to the solution so that its total volume was 30 mL. A piece of the as-prepared β-FeOOH nanorod-array film was placed in this mixture and then treated at 220 °C for 18 h to fabricate the Sn-doped hematite films. A red film formed after hydrothermal treatment. The film was washed with distilled H_2O and dried at room temperature for further use. Sn doping levels were tuned by adjusting the concentrations of the Sn colloidal solution. This parameter depended on laser ablation time.

For PEC measurements, the Sn-doped hematite films were annealed at temperatures that ranged from 0 to 750 °C at a heating rate of 2 °C min^{-1} held for 2 h. Thereafter, the samples were naturally cooled down to room temperature.

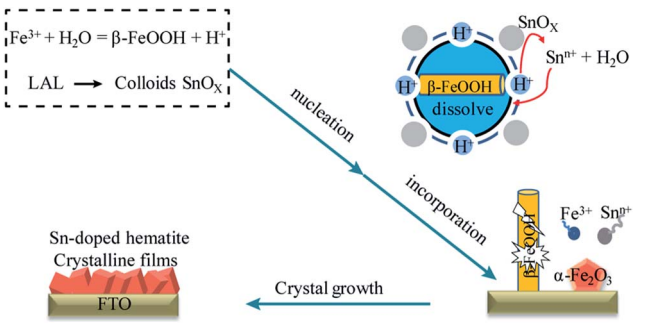

Scheme 1 Synthesis of Sn-doped hematite films through hydrothermal method.

Characterization

The X-ray diffraction (XRD) patterns of hematite films were obtained using a Philips X'Pert system with Cu Kα radiation (λ = 1.5419 Å, scanning rate 1° min^{-1}). Scanning electron microscopy (SEM) images were obtained using a Hitachi S-4800 focused-ion beam system. A transmission electron microscopy (TEM) system (JEOL, JEM-2010) with a 200 kV acceleration voltage was used to obtain the structural information of the products. X-ray photoelectron spectroscopy (XPS) analyses were performed on a Thermo ESCALAB 250 spectrometer equipped with an Al Kα X-ray source and calibrated using C 1s = 284.6 eV. The optical properties of the Sn-doped hematite films were studied using a UV-vis spectrophotometer (Solid 3700). The hematite nanostructures were converted to photoanodes by soldering a copper wire to a bare portion of an FTO substrate. All the edges of the substrate except the working area were sealed with epoxy resin. The dark and photocurrent were obtained using a Volta lab potentiostat in a three-electrode configuration with 1 M of NaOH (pH = 13.6) as the electrolyte, Ag/AgCl saturated KCl as the reference electrode, and a platinum wire as the counter electrode. *J–V* measurements of the α-Fe_2O_3 films were performed in an electrochemical workstation (Model CHI 660D, CH instruments, Inc., Austin, TX). The potential was swept at 25 mV s^{-1} from −0.5 V to 0.8 V. The source of white light used was AM 1.5 sunlight (450 W xenon lamp, 100 mW cm^{-2}). Electrochemical impedance spectroscopy (EIS) measurement was conducted in the same workstation with a frequency range of 0.01 kHz to 100 kHz at a potential of 1.23 *vs.* RHE.

Results and discussion

Fig. 1 shows the SEM images of Sn-doped hematite photoanodes. The films were composed of several irregular blobs in

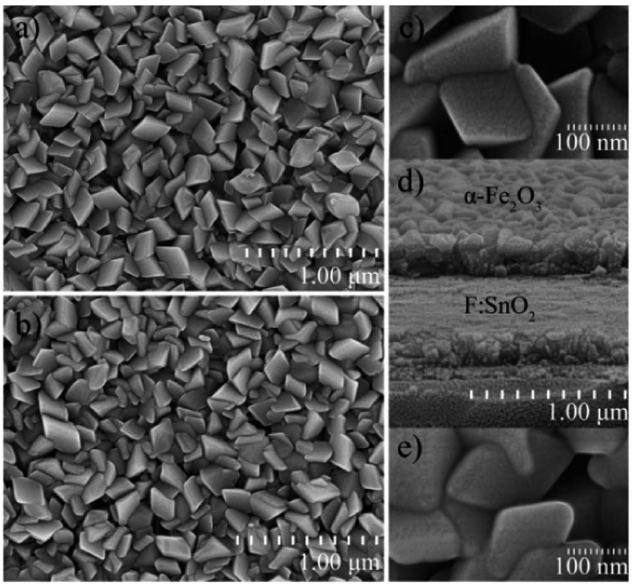

Fig. 1 SEM images of Sn–Fe_2O_3 film grown on an FTO conducting glass: (a) before annealing, (b) annealed at 750 °C for 2 h, (c) and (e) magnified image of (a) and (b), respectively, and (d) cross section of a 220 nm-thick Sn-doped hematite film.

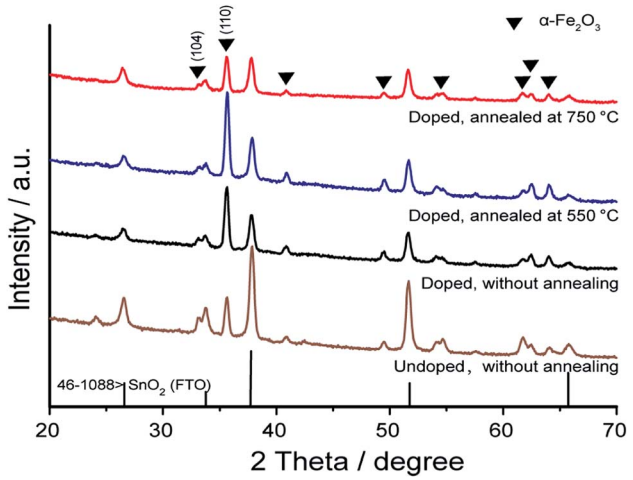

Fig. 2 XRD patterns of Sn–Fe_2O_3 films prepared under different conditions.

the Stranski–Krastanov growth (layer-plus-island growth) model. The as-deposited (Fig. 1a and c) and annealed (Fig. 1b and e) Sn-doped hematite films did not exhibit significant changes in their morphology. However, the grain edges and corners of the Sn-doped hematite became blurred after treatment at 750 °C. This phenomenon was observed in the magnified SEM images (Fig. 1c and e). High-temperature annealing enabled the crystal edges to form a stable structure instead of unstable sharp edges. The hematite layer exhibited a thickness of about 220 nm, as shown in Fig. 1d.

The influence of Sn impurities and annealing temperature on the α-Fe_2O_3 nanostructure and chemical bonding configuration were investigated. Fig. 2 and 4 show the XRD and XPS measurements of the Sn-doped hematite nanostructures, respectively. As shown in Fig. 2, both the undoped and Sn-doped hematite films display α-Fe_2O_3 in rhombohedral structure (space group: $R\bar{3}c$, JCPDS reference pattern 33-0664). Compared with the standard hematite pattern, the diffraction intensity of (110) plane is stronger than the (104) plane. This suggests that the hematite crystalline preferred growth alone the [110] direction on the substrate and it is desirable because the axis along which the electron mobility is greatest in hematite crystalline.[31] Fig. 3a is the TEM image of an individual Sn-doped hematite crystalline, which display the nanopolyhedron appear to be rhombohedral shape with a size about 150 nm. The HRTEM image (Fig. 3b) and corresponding SAED pattern (Fig. 3c) of the boxed area indicate that the lattice fringes fit well to the α-Fe_2O_3 (110) and (104) planes, the angle between (110) and (104) planes is 56.8°, which is in well fitted with the theoretical data and also our XRD analysis.

EDX analysis did not produce an accurate calculation of the Sn content in the film because of the influence of Sn atoms present in the FTO substrate. However, XPS with low photoelectron-escape depth (about 5 nm) was able to confirm the concentration of Sn in the resulting films. This process was performed without disturbing the FTO. XPS analyses were performed in the samples with or without annealing at 750 °C. As seen in the high-resolution XPS spectra of Fe 2p (Fig. 4a), the binding energies of Fe $2p^{1/2}$ and Fe $2p^{3/2}$ appear at 724.5 and 710.9 eV, respectively, with a satellite peak at 719.3 eV. This energy is characteristic of Fe^{3+} in α-Fe_2O_3. And in Fig. 4b, there were two peaks centered at 494.6 and 486.2 eV; these peaks corresponded to the Sn $3d_{3/2}$ and Sn $3d_{5/2}$ binding energy, respectively. The peak at 486.2 eV was caused by SnO_2 and a mixture of SnO_2 and SnO_x ($x < 2$) because the Sn $3d_{5/2}$ binding energy for pure SnO_2 was reported as 486.6 eV.[32] A doping source produced *via* LAL is nonstoichiometric SnO_x.[33] The XPS results showed the same type of SnO_x produced. The intensity of the Sn 3d binding energy of the Sn-doped hematite increased after annealing at 750 °C. Similar to XRD analysis, this behavior was caused by a small amount of Sn atoms that precipitated on the surface during high-temperature calcination. These atoms were produced by the doped hematite crystals and FTO layer.[34]

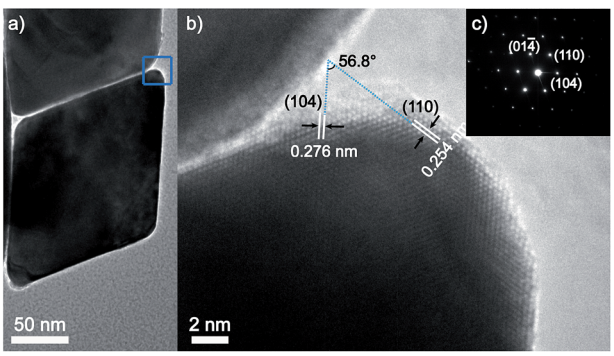

Fig. 3 Sn-doped hematite: (a) low-magnification TEM image, (b and c) HRTEM image and SAED pattern of the boxed area in the edge of crystal.

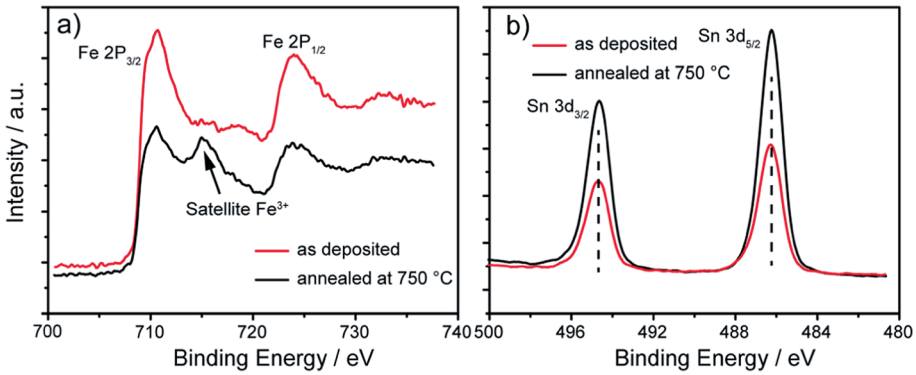

Fig. 4 X-ray photoelectron spectrum of: (a) Fe 2p and (b) Sn 3d obtained from Sn–Fe_2O_3 thin film sintered at 0 and 750 °C.

The UV-vis spectra of the Sn-doped hematite films were also obtained, as shown in Fig. 5a. The transmittance spectra of all the photoelectrodes annealed at different temperatures did not change after thermal treatment. The indirect optical band gaps in Sn-doped hematite were estimated by calculating the intercept of an extrapolated linear fit to the experimental date of a plot of $(-\ln T)^n$ (T is the transmission value, $n = 2$ for direct band gap and $n = 0.5$ for indirect optical band gap) *versus* the incident photo energy,[35] as shown in Fig. 5b. The indirect optical band gap of the Sn-doped film was 2.11 eV. This value coincided with reported values that ranged from 1.9 eV to 2.2 eV. The different values obtained in previous studies were due to differences in preparation method and indirect absorption process of pure-phase hematite.[36]

The effect of annealing temperature on the PEC performance of Sn-doped hematite photoanodes was investigated in 1 M of NaOH solution under one sun (AM 1.5 G) irradiation. Dark currents were not detected because they were extremely low. The potential values of the Ag/AgCl used in this study were converted to a RHE scale because photocurrent values in other studies were obtained under standard conditions (1.23 V *vs.* RHE). This process was performed using the Nernst relationship, as shown below:

$$E_{\mathrm{RHE}} = E_{\mathrm{Ag/AgCl}} + 0.059\mathrm{pH} + E^{\circ}_{\mathrm{Ag/AgCl}}$$

The current densities of the as-synthesized and annealed α-Fe_2O_3 were measured, as shown in Fig. 6. The FTO conductive layer was damaged when the annealing temperature was higher than 750 °C. Therefore, products annealed at temperatures higher than 750 °C were not investigated. The photocurrent densities of the α-Fe_2O_3 photoelectrodes changed after annealment. The highest photocurrent value was obtained for the film treated at 750 °C for 2 h; its value was 0.48 mA cm^{-2} at 1.23 V (*vs.* RHE). The as-deposited α-Fe_2O_3 exhibited the lowest photocurrent density at 0.02 mA cm^{-2}. Low-temperature annealing produced good crystalline structures and few film defects, thus enhancing the PEC performance. When the annealing temperature was increased up to 600 °C, a decrease in the photocurrent density was observed. This finding was due to increased particle size and precipitation of impurities from the host lattice. Consequently, the amount of recombination center increased. This result was described and partly confirmed in previous studies. The photoelectric properties initially improved and became varied when annealing temperature was increased.[37] However, the photocurrent of the as-prepared photoelectrodes in this study was maintained even at increasing annealing temperatures.

Electrochemical impedance spectroscopy (EIS) measurements were performed to obtain further evidence of the influence of annealing temperature on the PEC performance of hematite photoanodes. Measurements were performed under

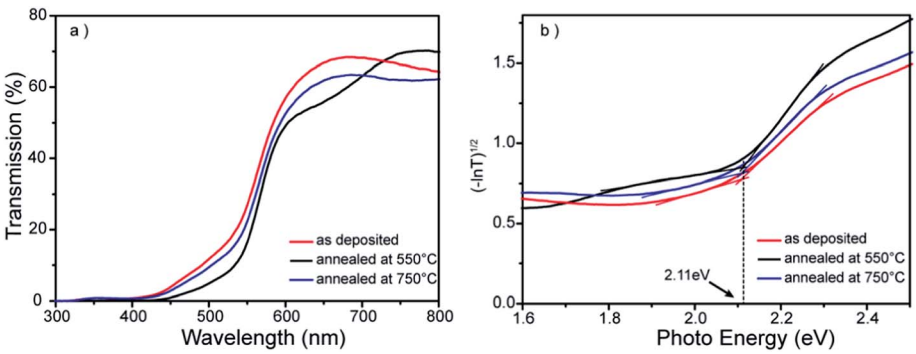

Fig. 5 (a) Transmission spectra of Sn–Fe_2O_3 films with different thermal treatments and (b) $(-\ln T)^2$ *vs.* photon energy ($h\nu$) plots of corresponding films.

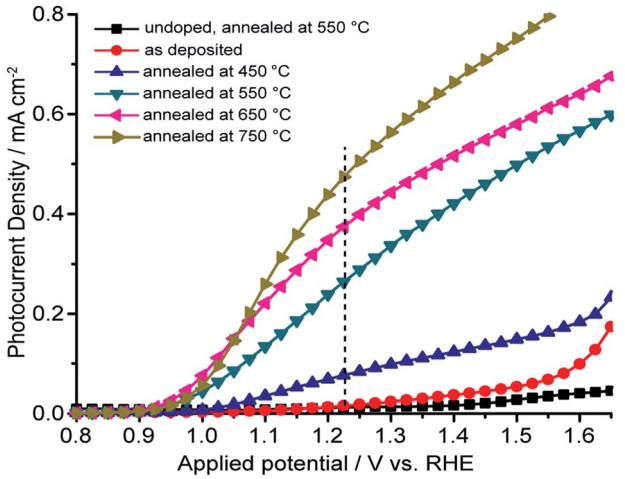

Fig. 6 Photocurrent density of Sn–Fe_2O_3 photoanodes annealed at different temperatures under one sun (AM 1.5 G) illumination in 1 M of NaOH electrolyte solution.

the same condition of gas evolution (at 1.23 V *vs.* RHE, 1 M of NaOH solution) under one sun irradiation. Fig. 7 shows the Nyquist plots of the photoanodes annealed at different temperatures, where the points were measured values and the solid curves were fitted results of an equivalent RC-circuit model (inset). The values of the elements obtained by fitting results are presented in Table 1. This table contains data on charge-transfer resistance (R) across the interfaces in the photoanode and constant phase elements (CPE) in parallel. The dates for all photoanodes fitted well with the two-RC circuit model but not with the classic three-RC circuit model for pure hematite films. Previous studies showed that three-RC circuits were assigned to Fe_2O_3||electrolyte (R_3), Fe_2O_3 film (R_2), and Fe_2O_3||FTO (R_1), respectively.[38,39] Since the electrode film were grown *in situ* in a hydrothermal process and the interface resistance of Fe_2O_3||FTO was very small and negligible. R_1 is not considered here in calculation.

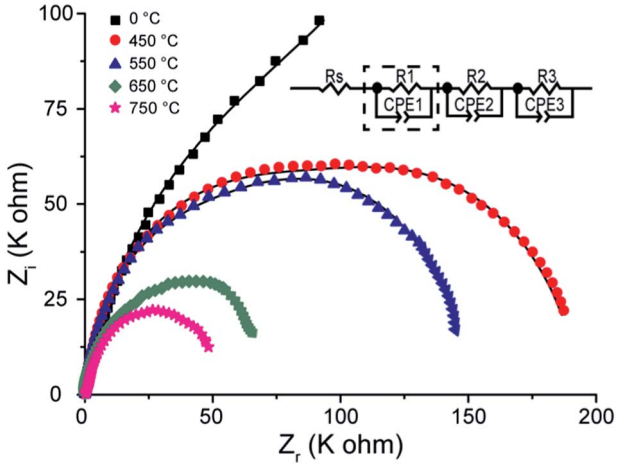

Fig. 7 Nyquist plots of Sn–Fe_2O_3 photoanodes. Points are measured values and solid curves are fitted lines. The inset shows the equivalent circuit.

Table 1 Fitted values of the equivalent circuit model in Fig. 7

(R/ohm) (CPE/F)	R_s	R_1 CPE_1	R_2 CPE_2	R_3 CPE_3
0 °C	21.33		9463 3.11×10^{-6}	71 046 8.71×10^{-6}
450 °C	12.88		8333 1.48×10^{-6}	11 062 8.89×10^{-6}
550 °C	9.28		5376 1.82×10^{-7}	9522 3.75×10^{-6}
650 °C	11.11		290.6 2.73×10^{-8}	5641 1.07×10^{-7}
750 °C	21.91		86.84 1.46×10^{-6}	5248 1.10×10^{-6}

R_S is the sheet resistance in a half-cell test system for EIS. The obtained R_s values were similar because of the same test conditions employed. However, the values for R_2 and R_3 changed significantly. The R_2 originated from the charge distribution among doped-Fe_2O_3 crystals. Table 1 shows that R_2 decrease sharply as the annealing temperature increased. The Mott–Schottky curves (Fig. S2†) also show that the slope of photoanode is reduced after thermal treatment, reflecting the significantly increase of carrier concentration. High concentration free electrons indicate the rapid and efficient separation of the photo-generated carrier. R_3/CPE_3, the largest semicircle corresponds to Fe_2O_3||electrolyte interface in the PEC systems, is closely related to the holes transfer. The holes generated by photo-excitation are transmitted to the anode surface, and O_2 can be produced during water splitting. As the Table 1 showing, R_3 also decreased with annealing temperature increasing. R_3 of the Sn-doped hematite photoanode annealed at 750 °C decreased by more than 100 times compared with that of the untreated hematite photoanodes. Here, the improved crystallinity after annealing treatment and the preferred (110) plane in the doped crystalline film are favor for the migration of electrons and holes to electrode surfaces, which should be main contributions to the significantly decrease of R_2 and R_3 and enhanced PEC performance. Moreover, Hamann *et al.*[40] demonstrated that annealing at elevated temperature can further remove the deleterious surface states of hematite. Ling *et al.*,[13] also proposed that Sn-doping improves the free electron density of hematite.

Conclusions

Photoelectrode consisting of Sn-doped hematite were prepared *in situ* on FTO substrates using a unique precursor of Sn colloidal species that produced *via* a liquid-phase laser ablation process. Annealment effects on PEC performance of Sn-doped hematite was investigated by evaluating the photocurrent and interfacial resistance. The Sn-doped hematite film with preferred growth orientation alone the [110] direction exhibited the highest photocurrent (0.48 mA cm^{-2} at 1.23 V *vs.* RHE) after being annealed at 750 °C. The improved crystallinity and the preferred (110) plane in the doped crystalline film facilitate the migration of electrons and holes to electrode surfaces, the remove of the deleterious surface states and increase of the free electron density. Those aspects should be main contributions to the significantly decrease of interfacial resistance and the enhanced PEC performance of Sn-doped hematite crystalline film.

Acknowledgements

This work was supported by the National Basic Research Program of China (2014CB931704), the National Natural Science Foundation of China (NSFC, no. 11174287, 51371166, 11204308) and the Instrument Developing Project of the Chinese Academy of Sciences under Grant no. YG2012065.

Notes and references

1 D. K. Bora, A. Braun and E. C. Constable, *Energy Environ. Sci.*, 2013, **6**, 407–425.
2 A. Fujishima and K. Honda, *Nature*, 1972, **238**, 37–38.
3 A. Kay, I. Cesar and M. Gratzel, *J. Am. Chem. Soc.*, 2006, **128**, 15714–15721.
4 Z. Li, W. Luo, M. Zhang, J. Feng and Z. Zou, *Energy Environ. Sci.*, 2013, **6**, 347.
5 V. M. Aroutiounian, V. M. Arakelyan and G. E. Shahnazaryan, *Sol. Energy*, 2005, **78**, 581–592.
6 A. B. Murphy, P. R. F. Barnes, L. K. Randeniya, I. C. Plumb, I. E. Grey, M. D. Horne and J. A. Glasscock, *Int. J. Hydrogen Energy*, 2006, **31**, 1999–2017.
7 K. Sivula, F. Le Formal and M. Gratzel, *ChemSusChem*, 2011, **4**, 432–449.
8 I. Cesar, A. Kay, J. A. G. Martinez and M. Gratzel, *J. Am. Chem. Soc.*, 2006, **128**, 4582–4583.
9 A. Duret and M. Gratzel, *J. Phys. Chem. B*, 2005, **109**, 17184–17191.
10 A. Fujimori, M. Saeki, N. Kimizuka, M. Taniguchi and S. Suga, *Phys. Rev. B: Condens. Matter Mater. Phys.*, 1986, **34**, 7318–7333.
11 J. H. Kennedy and K. W. Frese, *J. Electrochem. Soc.*, 1978, **125**, 709–714.
12 C. X. Kronawitter, I. Zegkinoglou, C. Rogero, J. H. Guo, S. S. Mao, F. J. Himpsel and L. Vayssieres, *J. Phys. Chem. C*, 2012, **116**, 22780–22785.
13 Y. C. Ling, G. M. Wang, D. A. Wheeler, J. Z. Zhang and Y. Li, *Nano Lett.*, 2011, **11**, 2119–2125.
14 J. Brillet, M. Gratzel and K. Sivula, *Nano Lett.*, 2010, **10**, 4155–4160.
15 D. K. Bora, A. Braun, R. Erni, G. Fortunato, T. Graule and E. C. Constable, *Chem. Mater.*, 2011, **23**, 2051–2061.
16 P. L. Liao, M. C. Toroker and E. A. Carter, *Nano Lett.*, 2011, **11**, 1775–1781.
17 C. J. Sartoretti, B. D. Alexander, R. Solarska, W. A. Rutkowska, J. Augustynski and R. Cerny, *J. Phys. Chem. B*, 2005, **109**, 13685–13692.
18 U. Bjorksten, J. Moser and M. Gratzel, *Chem. Mater.*, 1994, **6**, 858–863.
19 J. Liu, C. H. Liang, H. M. Zhang, Z. F. Tian and S. Y. Zhang, *J. Phys. Chem. C*, 2012, **116**, 4986–4992.
20 P. Zhang, A. Kleiman-Shwarsctein, Y. S. Hu, J. Lefton, S. Sharma, A. J. Forman and E. McFarland, *Energy Environ. Sci.*, 2011, **4**, 1020–1028.
21 C. Leygraf, M. Hendewerk and G. A. Somorjai, *J. Catal.*, 1982, **78**, 341–351.
22 J. A. Glasscock, P. R. F. Barnes, I. C. Plumb and N. Savvides, *J. Phys. Chem. C*, 2007, **111**, 16477–16488.
23 Y. S. Hu, A. Kleiman-Shwarsctein, G. D. Stucky and E. W. McFarland, *Chem. Commun.*, 2009, 2652–2654.
24 J. Liu, C. H. Liang, G. P. Xu, Z. F. Tian, G. S. Shao and L. D. Zhang, *Nano Energy*, 2013, **2**, 328–336.
25 J. H. Kennedy, M. Anderman and R. Shinar, *J. Electrochem. Soc.*, 1981, **128**, 2371–2373.
26 J. Frydrych, L. Machala, J. Tucek, K. Siskova, J. Filip, J. Pechousek, K. Safarova, M. Vondracek, J. H. Seo, O. Schneeweiss, M. Gratzel, K. Sivula and R. Zboril, *J. Mater. Chem.*, 2012, **22**, 23232–23239.
27 V. M. Aroutiounian, V. M. Arakelyan, G. E. Shahnazaryan, H. R. Hovhannisyan, H. L. Wang and J. A. Turner, *Sol. Energy*, 2007, **81**, 1369–1376.
28 N. T. Hahn and C. B. Mullins, *Chem. Mater.*, 2010, **22**, 6474.
29 K. Sivula, R. Zboril, F. Le Formal, R. Robert, A. Weidenkaff, J. Tucek, J. Frydrych and M. Gratzel, *J. Am. Chem. Soc.*, 2010, **132**, 7436–7444.
30 L. F. Xi, S. Y. Chiam, W. F. Mak, P. D. Tran, J. Barber, S. C. J. Loo and L. H. Wong, *Chem. Sci.*, 2013, **4**, 164–169.
31 A. Kay, I. Cesar and M. Gratzel, *J. Am. Chem. Soc.*, 2006, **128**, 15714–15721.
32 Y. Q. Cao, T. He, L. S. Zhao, E. J. Wang, W. S. Yang and Y. A. Cao, *J. Phys. Chem. C*, 2009, **113**, 18121–18124.
33 C. H. Liang, Y. Shimizu, T. Sasaki and N. Koshizaki, *J. Phys. Chem. B*, 2003, **107**, 9220–9225.
34 R. Morrish, M. Rahman, J. MacElroy and C. A. Wolden, *ChemSusChem*, 2011, **4**, 474–479.
35 M. L. Zhang, W. J. Luo, Z. S. Li, T. Yu and Z. G. Zou, *Appl. Phys. Lett.*, 2010, 97.
36 A. A. Tahir, K. G. U. Wijayantha, S. Saremi-Yarahmadi, M. Mazhar and V. Mckee, *Chem. Mater.*, 2009, **21**, 3763–3772.
37 S. H. Tamboli, G. Rahman and O.-S. Joo, *J. Alloys Compd.*, 2012, **520**, 232–237.
38 J. Young Kim, J.-W. Jang, D. Hyun Youn, J. Yul Kim, E. Sun Kim and J. Sung Lee, *RSC Adv.*, 2012, **2**, 9415.
39 H. Jun, B. Im, J. Y. Kim, Y.-O. Im, J.-W. Jang, E. S. Kim, J. Y. Kim, H. J. Kang, S. J. Hong and J. S. Lee, *Energy Environ. Sci.*, 2012, **5**, 6375.
40 O. Zandi and T. W. Hamann, *J. Phys. Chem. Lett.*, 2014, **5**, 1522–1526.